Initial development of the DIII–D snowflake divertor control

E. Kolemen[1], P.J. Vail[1], M.A. Makowski[2], S.L. Allen[2], B.D. Bray[3],
M.E. Fenstermacher[2], D.A. Humphreys[3], A.W. Hyatt[3], C.J. Lasnier[2],
A.W. Leonard[3], A.G. McLean[2], R. Maingi[1], R. Nazikian[1], T.W. Petrie[3],
V.A. Soukhanovskii[2] and E.A. Unterberg[4]

[1] Princeton University, Princeton, NJ 08544, United States of America
[2] Lawrence Livermore National Laboratory, Livermore, CA 94550, United States of America
[3] General Atomics, San Diego, CA 92186, United States of America
[4] Oak Ridge National Laboratory, Oak Ridge, TN 37831, United States of America

E-mail: ekolemen@princeton.edu

Abstract

Simultaneous control of two proximate magnetic field nulls in the divertor region is
demonstrated on DIII–D to enable plasma operations in an advanced magnetic configuration
known as the snowflake divertor (SFD). The SFD is characterized by a second-order poloidal
field null, created by merging two first-order nulls of the standard divertor configuration. The
snowflake configuration has many magnetic properties, such as high poloidal flux expansion,
large plasma-wetted area, and additional strike points, that are advantageous for divertor heat
flux management in future fusion reactors. However, the magnetic configuration of the SFD
is highly-sensitive to changes in currents within the plasma and external coils and therefore
requires complex magnetic control. The first real-time snowflake detection and control system
on DIII–D has been implemented in order to stabilize the configuration. The control algorithm
calculates the position of the two nulls in real-time by locally-expanding the Grad–Shafranov
equation in the divertor region. A linear relation between variations in the poloidal field coil
currents and changes in the null locations is then analytically derived. This formulation allows
for simultaneous control of multiple coils to achieve a desired SFD configuration. It is shown
that the control enabled various snowflake configurations on DIII–D in scenarios such as
the double-null advanced tokamak. The SFD resulted in a 2.5× reduction in the peak heat
flux for many energy confinement times (2–3 s) without any adverse effects on core plasma
performance.

Keywords: advanced divertor, divertor, control, snowflake, DIII-D

(Some figures may appear in colour only in the online journal)

1. Introduction

Future tokamaks will require robust technologies for the mitigation of heat exhaust onto plasma-facing components (PFCs). The present strategy for heat flux management in tokamaks such as ITER [1, 2], FNSF [3, 4], and DEMO [1, 5] includes the use of an axisymmetric magnetic divertor with a first-order magnetic field null (referred to hereafter as the standard divertor) that directs plasma which has escaped confinement onto divertor surfaces designed for exposure to high heat fluxes. A generally-accepted design criterion, determined by the limitations of candidate PFC materials, is that the steady-state heat flux on the divertor should not exceed $\sim$10 MW m^{-2} in order to prevent significant erosion of divertor surfaces. To adhere to this limit, next-generation devices operating in a standard divertor configuration will require the use of a range of additional technologies. It is well-known that ITER must operate in a stable detached regime with significant radiation from the plasma boundary ($\sim$70% of the total exhausted power), and reactor-relevant
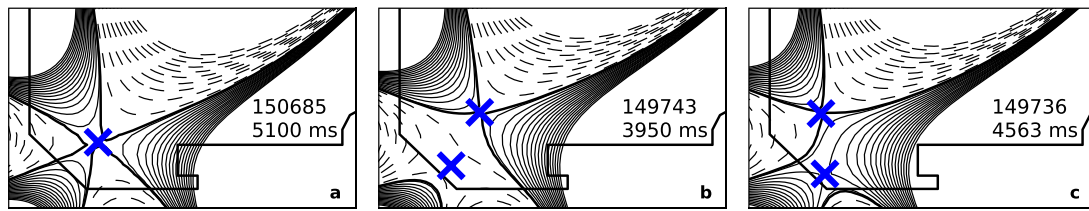
Figure 1. Three plasma equilibria on DIII–D showing (*a*) the exact snowflake configuration with a second-order null, (*b*) the snowflake-plus configuration with a secondary null in the private flux region, and (*c*) the snowflake-minus configuration with a secondary null in the scrape-off layer.

devices such as DEMO will demand more aggressive measures.

In recent years, the use of alternative divertor configurations, known as advanced divertors, has been proposed as a promising means of reducing the peak heat flux onto divertor surfaces in next-generation devices such as DEMO. Examples of advanced magnetic divertors are the various snowflake divertor (SFD) configurations [6], X-divertor [7], super X-divertor [8], and X-point target divertor [9]. The concept underlying each of these divertor configurations is to modify the magnetic geometry of the standard divertor in ways which are advantageous for heat flux mitigation. The X-divertor and some SFD configurations aim to reduce the peak heat flux by introducing a secondary poloidal field null near the outer strike point, thereby increasing the flux expansion and plasma-wetted area. Other variants of the SFD configuration are characterized by lower poloidal field magnitude in the null region, leading to a longer X-point connection length and a corresponding increase in volumetric power losses. Concepts such as the super-X divertor rely upon a significant increase in the radius of the outer strike point. The magnetic topology of a specific advanced divertor configuration may be characterized by several of these properties simultaneously.

Recent research on the DIII–D tokamak has focused on investigating the physics of the snowflake divertor. This divertor concept has previously been explored on tokamaks such as TCV [10], NSTX [11], and EAST [12] and is being considered for next-generation devices such as DEMO [13] and CFETR [14]. The SFD is characterized by a second-order poloidal field null, created by merging two first-order nulls of the standard divertor configuration. This configuration is known as the exact snowflake as the flux surfaces near the null point have a hexagonal structure that is reminiscent of a snowflake. The magnetic geometry of the snowflake is quite sensitive to changes in currents within the plasma and external coils [6, 15]. As such, one of two alternative configurations is typically observed: (1) the snowflake-plus configuration with a primary null on the separatrix and a secondary null in the private flux region, and (2) the snowflake-minus configuration in which the secondary null lies in the scrape-off layer. Figure 1 depicts three plasma equilibria that are representative of the achievable snowflake configurations on DIII–D.

Due to the sensitive nature of the SFD configuration and the large range of potential magnetic geometries, feedback control is required to regulate the configuration during real-time plasma operations. Magnetic control of the plasma shape and divertor geometry on DIII–D is generally accomplished

using the isoflux shape control algorithm [16] combined with real-time equilibrium reconstructions computed by the rtEFIT algorithm [17]. The isoflux algorithm regulates the shape of the plasma boundary by using magnetic coils to minimize the errors between the magnetic flux at selected points on the desired boundary and the flux at a reference point. For plasmas in a single-null or double-null divertor configuration, this reference flux is generally chosen to be the flux at a magnetic field null. The radial and vertical coordinates of the null are controlled directly using a set of dedicated divertor control coils. While simple and well-developed, the isoflux control scheme at DIII–D, as well as other standard plasma control strategies as described in [18–20] and the references therein, does not easily generalize to control of SFD configurations. For instance, the number of independent parameters required for control of the two null locations exceeds the number of actuators made available for their control by the mostly single-input–single-output isoflux algorithm. This underactuated system therefore requires a more sophisticated multiple-input-multiple-output method for computing the actuator requests needed to achieve a desired snowflake geometry. Furthermore, the iterative method used by rtEFIT for real-time null location, while sufficient for most standard divertor discharges, does not extend easily to the location of two closely-spaced nulls in the snowflake configuration. These challenges warrant the investigation of more advanced techniques for control of the snowflake divertor. In this paper, we present the development and implementation of one such control system at DIII–D that enabled plasma operations in a variety of SFD configurations. In section 2, we discuss the details of the algorithm, which is designed to locate the two magnetic field nulls of the SFD and compute coil currents required to achieve a desired configuration. In section 3, we present the results of DIII–D experiments that provided initial verification of controller performance. Finally, in section 4, we summarize our results and identify aspects of the control algorithm that require further development.

2. Snowflake control algorithm

Control of the plasma poloidal shape and position on DIII–D is accomplished using a set of toroidally axisymmetric magnetic coils that surround the vacuum vessel. The coils are connected in series with pulse-width modulated (chopper) power supplies that provide the voltages necessary for achieving a desired plasma shape. The chopper commands for the power supplies are computed in a feedback loop by algorithms that
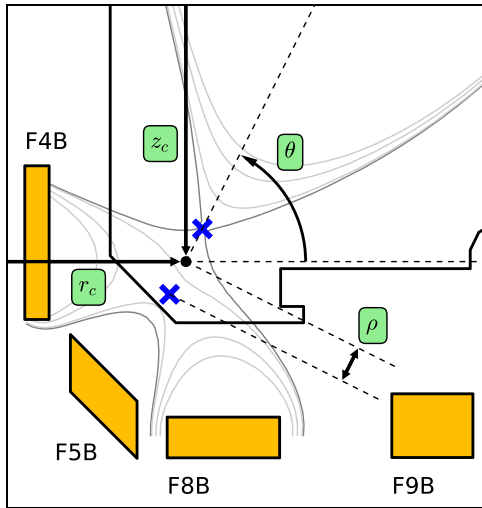
Figure 2. Illustration of the lower divertor on DIII–D showing the limiter surface, the poloidal field coils available for snowflake divertor (SFD) control, and the four parameters used to specify the geometry of the SFD magnetic configuration in the control system.

have been designed for achieving a variety of shape control objectives. In this section, we present an algorithm, designed to function in parallel with the isoflux shape control algorithm, that has been developed for feedback control of the SFD configuration. Using data obtained from real-time reconstructions of the plasma equilibria provided by rtEFIT, the algorithm computes the coil currents required for obtaining a desired SFD magnetic geometry. On DIII–D, several poloidal field coils are effective actuators for the snowflake configuration, as shown in figure 2. We select the F4B, F5B, and F8B coils as actuators for the control system described in this paper. The F9B coil is also effective at manipulating the SFD. However, the current in this coil is typically set to zero throughout a plasma discharge in order to prevent the outer strike point from entering the cryopump gap (which could cause significant damage to the unprotected surfaces within the cryopump).

For the remainder of this section, we discuss the major components of the snowflake control algorithm that has been implemented within the DIII–D plasma control system (PCS), as is shown in figure 3. We omit a discussion of the rtEFIT algorithm, which has been described extensively elsewhere. The snowflake control scheme is built upon a linearized relation between variations in the control coil currents and changes in the two null point positions, a relation which is updated continuously every ∼1 ms as the SFD configuration evolves. In section 2.1, we describe a procedure, based upon a series expansion of flux and field, that provides simple analytical expressions which are then used in section 2.2 to obtain the desired linearized relation. As the rtEFIT algorithm at DIII–D is currently not configured to simultaneously locate two nearby magnetic field nulls, we also use the series expansion to approximate the locations of the two SFD nulls in real-time. In section 2.3, we provide expressions for the null point locations and assess their accuracy. Finally, in section 2.4, we describe the controller which is used for achieving the desired coil currents.

2.1. Approximate the magnetic field structure

The first task of the control algorithm is to approximate the geometry of the magnetic flux surfaces in the divertor region. Under the assumption that the current density in the divertor region is small and therefore can be neglected, the Grad–Shafranov equation reduces to the following,

$$(r_0 + x)\frac{\partial}{\partial x}\left(\frac{1}{r_0 + x}\frac{\partial \psi}{\partial x}\right) + \frac{\partial^2 \psi}{\partial v^2} = 0, \qquad (1)$$

where $\psi(x, v)$ is the poloidal magnetic flux function, x is the radial coordinate relative to the position r_0, and v is the vertical coordinate relative to the position z_0. The radial position r_0 and vertical positon z_0 can be chosen arbitrarily subject to the constraint that this coordinate is close to the expected location of the SFD (roughly defined as the center of the two nulls). The required degree of closeness is such that the inequality, $|x|, |v| \ll r_0$, is satisfied throughout the region of interest. The flux function is related to the radial, B_r, and vertical, B_z, components of the magnetic field through the following relations,

$$B_r = -\frac{1}{r_0 + x}\frac{\partial \psi}{\partial v}, \qquad (2a)$$

$$B_z = \frac{1}{r_0 + x}\frac{\partial \psi}{\partial x}. \qquad (2b)$$

Following the approach taken by Ryutov *et al* [21], we seek a series solution to (1) of the form,

$$\psi(x, z) = l_1 x + l_2 v + q_1 x^2 + 2q_2 xv + q_3 v^2 + c_1 x^3 \\ + c_2 x^2 v + c_3 xv^2 + c_4 v^3, \qquad (3)$$

where we have neglected the zeroth-order terms as they do not contribute to the magnetic field components. Upon substituting (3) into (1) and setting the zeroth and first-order terms to zero, we obtain the following three constraints on the expansion coefficients,

$$-l_1 + 2q_1 r_0 + 2q_3 r_0 = 0, \qquad (4a)$$

$$2q_3 + 6c_1 r_0 + 2c_3 r_0 = 0, \qquad (4b)$$

$$-2q_2 + 2c_2 r_0 + 6c_4 r_0 = 0. \qquad (4c)$$

Furthermore, by substituting (3) into (2a) and (2b), we obtain expressions for the magnetic field components, B_r and B_z, in terms of the series expansion coefficients,

$$B_r = -\frac{1}{r_0 + x}(l_2 + 2q_2 x + 2q_3 v + c_2 x^2 + 2c_3 xv + 3c_4 v^2), \qquad (5a)$$

$$B_z = \frac{1}{r_0 + x}(l_1 + 2q_1 x + 2q_2 v + 3c_1 x^2 + 2c_2 xv + c_3 v^2). \qquad (5b)$$

We select as our independent parameters the coefficients l_1, l_2, q_2, q_3, c_1, and c_4 and then solve for the remaining three coefficients using (4a) through (4c),

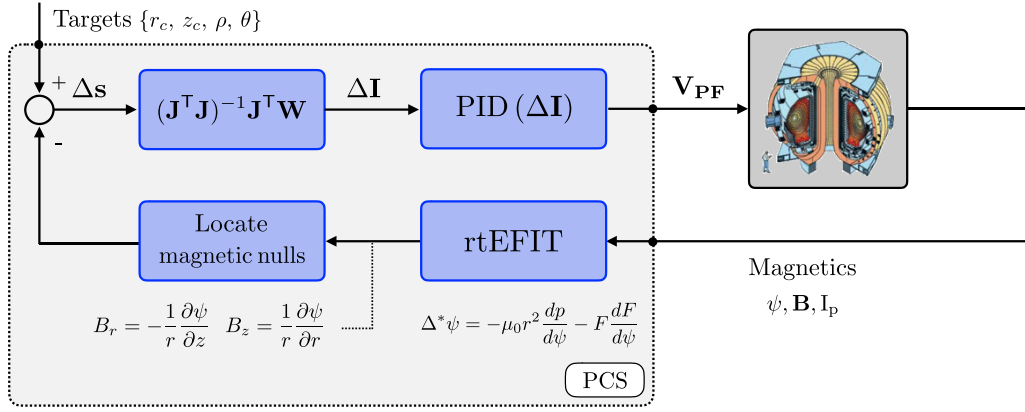$$q_1 = -q_3 + l_1/2, \qquad (6a)$$

$$c_2 = -3c_4 + q_2, \qquad (6b)$$

3

Figure 3. Major components of the snowflake control algorithm within the DIII–D plasma control system.

$$c_3 = -3c_1 - q_3. \tag{6c}$$

It is shown in [21] that the last terms on the right-hand sides of (6a) through (6c) are small and can be neglected. Substituting into (5a) and (5b), we obtain the following expressions for the magnetic field components in terms of the independent parameters,

$$B_r = -\frac{1}{r_0 + x}\left(l_2 + 2q_2x + 2q_3v - 3c_4\left(x^2 - v^2\right) - 6c_1xv\right), \tag{7a}$$

$$B_z = \frac{1}{r_0 + x}\left(l_1 - 2q_3x + 2q_2v + 3c_1\left(x^2 - v^2\right) - 6c_4xv\right). \tag{7b}$$

(7a) and (7b) for the field components are linear functions of the six independent expansion coefficients. The values of the coefficients can be easily determined, therefore, if we know the values of B_r and B_z at three points in the divertor region. At DIII–D, these values are obtained from the rtEFIT algorithm, which computes a new equilibrium, and thus new values for the magnetic field components, every ~ 1 ms. For the remainder of this section, we assume that the values of the six independent expansion coefficients are known.

2.2. Locate the magnetic nulls

After obtaining an approximate solution for the fluxes and fields in the divertor region, we locate the two magnetic field nulls that comprise the SFD. By definition, a magnetic null is a point at which $B_r = B_z = 0$. In order to locate the nulls, therefore, we set (7a) and (7b) equal to zero and solve for coordinate pairs (x, z). After some calculation, the details of which can be found in [21], we find the coordinates of the two null points in terms of the series expansion coefficients,

$$r_{\text{null}} = r_0 + \sigma_0 \pm \sqrt{\frac{P}{2} + \sqrt{\frac{P^2}{4} + Q^2}}, \tag{8a}$$

$$z_{\text{null}} = z_0 + \zeta_0 \pm \text{sign}\,(Q)\sqrt{-\frac{P}{2} + \sqrt{\frac{P^2}{4} + Q^2}}, \tag{8b}$$

where,

$$\sigma_0 = \frac{q_3c_1 + q_2c_4}{3\left(c_1^2 + c_4^2\right)}, \tag{9a}$$

$$\zeta_0 = \frac{q_2c_1 - q_3c_4}{3\left(c_1^2 + c_4^2\right)}, \tag{9b}$$

and,

$$P = \frac{l_2c_4 - l_1c_1}{3\left(c_1^2 + c_4^2\right)} + \sigma_0^2 - \zeta_0^2, \tag{10a}$$

$$Q = \frac{l_2c_1 + l_1c_4}{6\left(c_1^2 + c_4^2\right)} + \sigma_0\zeta_0. \tag{10b}$$

At DIII–D, the controlled parameters are not the two $(x_{\text{null}}, z_{\text{null}})$ coordinate pairs defined in (8a) and (8b) but rather a set of polar coordinates that are related to these variables as follows,

$$r_c = r_0 + \sigma_0, \tag{11a}$$

$$z_c = z_0 + \zeta_0, \tag{11b}$$

$$\rho = \sqrt{(r_{\text{null}}^+ - r_c)^2 + (z_{\text{null}}^+ - z_c)^2}, \tag{11c}$$

$$\theta = \tan^{-1}\left((z_{\text{null}}^+ - z_c)/(r_{\text{null}}^+ - r_c)\right), \tag{11d}$$

where r_{null}^+ and z_{null}^+ denote the values of (8a) and (8b) computed by taking the sum of the two terms on the right-hand sides. As shown in figure 2, r_c and z_c are the radial and vertical coordinates of the snowflake centroid, respectively, ρ is the radius of the snowflake (half the distance between the two nulls), and θ is the angular orientation of the snowflake relative to the horizontal. An angle between $0°$ and $90°$ denotes a snowflake-plus configuration (as is depicted in figure 2), while an angle between $0°$ and $-90°$ denotes a snowflake-minus configuration. Our choice of the four controlled parameters in (11a) through (11d) is somewhat arbitrary, and other parameters can be used for control of the configuration. We also note that while the algorithm computes the locations of the two nulls, it does not identify which of the two nulls is the primary null on the separatrix. This limitation of the algorithm has important consequences for the performance of the controller, as we will discuss further in sections 3 and 4.
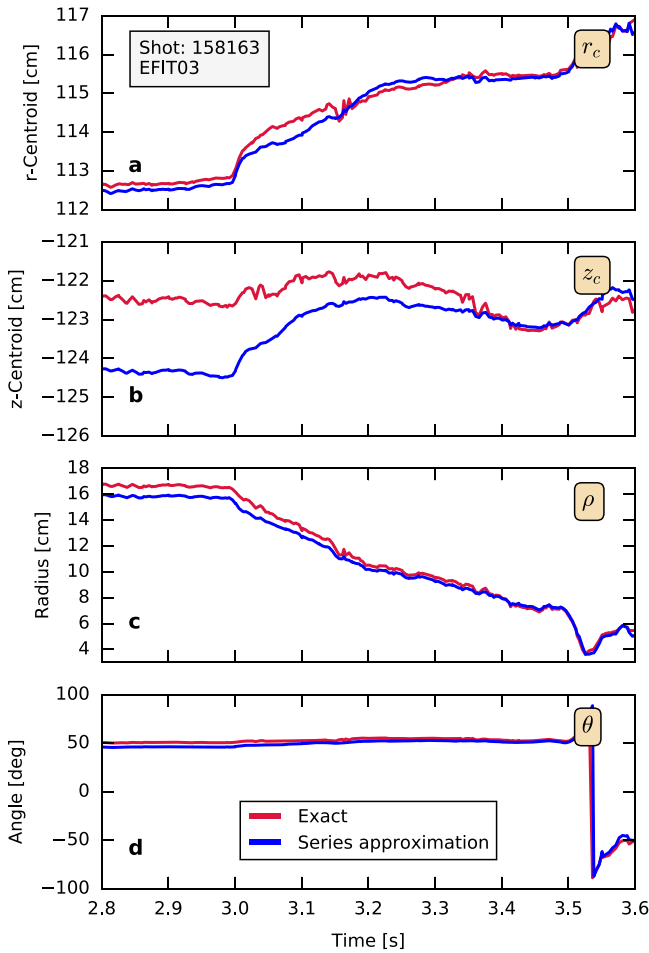
Figure 4. Comparison of the snowflake location for DIII–D shot 158163 as computed using the series expansion method presented in section 2 (blue) and as computed from a direct calculation of the two null point positions using an iterative procedure (red). Plotted in frames (*a*) through (*d*) are the snowflake centroid radial coordinate, centroid vertical coordinate, radius, and angle, respectively.

We emphasize that the null point locations given by (11*a*) through (11*d*) derive from a series expansion of the flux function and are therefore approximations of the actual null point locations. To assess the accuracy of these approximations, we display in figure 4(*a*) comparison of the snowflake location for DIII–D shot 158163 as computed by the series expansion approach and as computed by a direct calculation of the two null point locations using an iterative procedure. As seen in the figure, the series expansion provides a very good approximation of the snowflake location throughout the time-range shown, and the approximation becomes more accurate as the radius decreases and the configuration approaches a near-exact SFD. The series expansion method presented in this section therefore provides a reliable method for determining analytical expressions for the SFD location, especially for use in a feedback control system in which extreme accuracy is not of paramount importance.

After determining the parameters in (11*a*) through (11*d*), we compute a vector of snowflake position errors, $\Delta\mathbf{s}$, defined as,

$$\Delta\mathbf{s} = \begin{bmatrix} \Delta r_c \\ \Delta z_c \\ \Delta\rho \\ \Delta\theta \end{bmatrix}, \tag{12}$$

where the entries of the vector in (12) are the differences between the present and the target values of the snowflake parameters.

2.3. Compute the coil current requests

After determining the locations of the two magnetic nulls and computing the snowflake error vector, we proceed by calculating the coil currents that are required to achieve the desired snowflake configuration. These coil currents are determined by inverting the following equation,

$$\Delta\mathbf{s} = \mathbf{J}\Delta\mathbf{I}, \tag{13}$$

where $\Delta\mathbf{s}$ is defined in (12), $\Delta\mathbf{I}$ is a vector of current requests for the F4B, F5B, and F8B coils, and $\mathbf{J}$ is the Jacobian matrix of partial derivatives that quantifies the effect on the snowflake position of modifying the coil currents. The first step toward the determination of the required coil currents, therefore, is the calculation of the Jacobian matrix. The elements of $\mathbf{J}$ are as follows,

$$\mathbf{J} = \begin{bmatrix} \partial_\mathbf{I} r_c \\ \partial_\mathbf{I} z_c \\ \partial_\mathbf{I} \rho \\ \partial_\mathbf{I} \theta \end{bmatrix}, \tag{14}$$

where the operator $\partial_\mathbf{I}$ denotes partial differentiation with respect to each of the control coil currents. The dimensions of $\mathbf{J}$, therefore, are 4×3 as there are four controlled variables and three coils used to affect the control. Each row of $\mathbf{J}$ is computed separately according to the following equations,

$$\partial_\mathbf{I} r_c = \partial_\mathbf{x}\sigma_0 \cdot \partial_\mathbf{B}\mathbf{x} \cdot \partial_\mathbf{I}\mathbf{B}, \tag{15a}$$

$$\partial_\mathbf{I} z_c = \partial_\mathbf{x}\zeta_0 \cdot \partial_\mathbf{B}\mathbf{x} \cdot \partial_\mathbf{I}\mathbf{B}, \tag{15b}$$

$$\partial_\mathbf{I}\rho = (\partial_P\rho \cdot \partial_\mathbf{x}P + \partial_Q\rho \cdot \partial_\mathbf{x}Q) \cdot \partial_\mathbf{B}\mathbf{x} \cdot \partial_\mathbf{I}\mathbf{B}, \tag{15c}$$

$$\partial_\mathbf{I}\theta = (\partial_P\theta \cdot \partial_\mathbf{x}P + \partial_Q\theta \cdot \partial_\mathbf{x}Q) \cdot \partial_\mathbf{B}\mathbf{x} \cdot \partial_\mathbf{I}\mathbf{B}. \tag{15d}$$

The magnetic field matrix $\partial_\mathbf{I}\mathbf{B}$ contains terms of the form $\partial B_{r_i}/\partial I_j$ and $\partial B_{z_i}/\partial I_j$ for $i \in \{1, 2, 3\}$ and $j \in \{F4B, F5B, F8B\}$. The terms B_{r_i} and B_{z_i} for the values of the index i are the magnetic field components at the three points which were used to compute the values of the expansion coefficients in section 2.1. These partial derivatives are computed offline using the Green's function of the Grad–Shafranov problem and are loaded into the control system memory prior to a plasma discharge. The remainder of the derivatives in (15*a*) through (15*d*) are obtained through repeated use of the chain rule. We provide explicit expressions for these derivatives in the appendix. In this initial implementation of the control system on DIII–D, we account for the direct effect of the coils on the poloidal field using the

Green's function but neglect any effect which the plasma currents may have on the field. This choice was made to limit the complexity of the real-time implementation of the algorithm. We note that this simplistic model, when used in a feedback loop, is accurate enough to achieve many desired configurations, as will be shown in section 3.

After computing the Jacobian, we invert (13) using the matrix pseudoinverse in order to determine the coil currents,

$$\Delta \mathbf{I} = (\mathbf{J}^{\mathsf{T}}\mathbf{J})^{-1}\mathbf{J}^{\mathsf{T}}\mathbf{W}\Delta \mathbf{s}, \tag{16}$$

where $\mathbf{W}$ is a diagonal weighting matrix that allows the user to define the relative importance of the control of the four snowflake parameters. In (16), the components of $\Delta \mathbf{I}$ are the desired changes to be made to the present values of the currents in the control coils. The subsequent task of the controller is to achieve the desired coil currents based upon these requests.

2.4. Compute chopper commands with PID control

The final task of the algorithm is to convert the coil current requests computed in (16) to chopper commands for the poloidal field coil power supplies. The isoflux shape control algorithm within the PCS is configured to use proportional-integral-derivative (PID) controllers for the calculation of chopper voltage commands. PID is a generic feedback control law that attempts to minimize the error between the measured value of a system variable and a desired setpoint for that variable by applying a properly-chosen corrective action to the system [22, 23]. This corrective action, denoted as $u(t)$, is computed as,

$$u(t) = P \cdot e(t) + I/\tau_{\mathrm{I}} \cdot \int_0^t e(\tau)\,\mathrm{d}\tau + D \cdot \tau_{\mathrm{D}} \cdot \frac{\mathrm{d}e(t)}{\mathrm{d}t}, \tag{17}$$

where we have,

$$e(t) = r(t) - y(t), \tag{18}$$

the difference between the desired setpoint and the measured value of the system variable. In (17), the terms P, I, and D are the proportional, integral, and derivative gains, respectively, while τ_{I} and τ_{D} are time constants for the integral and derivative components. The form of the PID controller in (17) is the form implemented within the PCS, but other forms are commonly used in the control literature. In the isoflux control algorithm, the errors $e(t)$—the inputs to the PID controllers — are either the flux errors at selected points on the plasma boundary or errors in the magnetic null position(s). The outputs of the controller $u(t)$ are the chopper commands for the poloidal field coil power supplies.

When designing the controller for the snowflake configuration, we chose to use this existing infrastructure to compute our actuator requests. In our algorithm, the inputs to the PID controllers are the coil current requests that were obtained in (16). The outputs are the chopper commands for the coils used for snowflake control. Also required are the values of the controller gains and time constants. For the experiments that we describe in section 3, a proportional-only controller was used, and the values of the proportional gains were tuned empirically

during operations. We chose to use proportional-only control during the initial experiments primarily for reasons of simplicity. We note that control of the plasma boundary shape on DIII–D is generally accomplished with proportional-only control. Some limitations on the performance of the control due to the proportional-only control action will be discussed in section 3.

3. Initial experimental results on DIII–D

The control algorithm as described in section 2 was implemented in the DIII–D plasma control system and then tested offline using the data simserver, a utility that allows a PCS developer to run the control system in a simulation mode using the raw data from a previous plasma discharge as input to the PCS. The simserver therefore affords the developer a tool for debugging an algorithm offline using a simulated data stream. After the snowflake control implementation was tested with the simserver, the controller was deployed for use during real-time plasma operations. In this section, we present some initial results from the first experiments that employed the algorithm.

In figure 5, we show the results of DIII–D shot 159008 in which the snowflake control was used to achieve a near-exact SFD configuration with radius ~3 cm. We apply the term near-exact to any SFD configuration in which the magnetic nulls are contained within the zone of strong curvature-driven plasma convection around the primary null as first described in [24]. This so-called 'churning mode' is hypothesized to be a cause of the heat flux splitting among multiple divertor legs in the SFD configuration. Furthermore, the mode strongly perturbs the poloidal field in the convection zone (computed to be ~3 cm relative to the primary null for a typical DIII–D snowflake discharge). This places a natural limit on how well the configuration can be made to resemble the ideal second-order null of the exact snowflake.

As indicated in figure 5, the snowflake control was enabled at $t = 2.3$ s. Immediately prior to this time, the location of the primary magnetic null was controlled by the standard isoflux algorithm using the F4B and F8B coils, while the F5B coil was programmed to perform a pre-defined coil current ramp to -0.4 kA. When running a snowflake configuration experiment on DIII–D, the F5B coil operates at a negative polarity relative to the F4B and F8B coils, and the pre-programmed current ramp is used to move a secondary magnetic null into the vacuum vessel to form a quasi-snowflake configuration, as shown in figure 5(*f*). Once the secondary null is in the vacuum vessel, the snowflake control is enabled so as to move the SFD to the desired configuration. In shot 159008, the only controlled parameter was the snowflake radius, ρ, with a target value of 0 cm (an exact-SFD configuration), as indicated in figure 5(*a*). To designate ρ as the only controlled parameter in this scenario, the weighting matrix in (16) was programmed to have only one nonzero diagonal entry corresponding to the snowflake radius. As seen in the figure, the controller reduced and stabilized the snowflake radius near a value of 3 cm. The steady-state error between the snowflake radius and its target value as shown in figure 5(*a*) is due to the choice of using
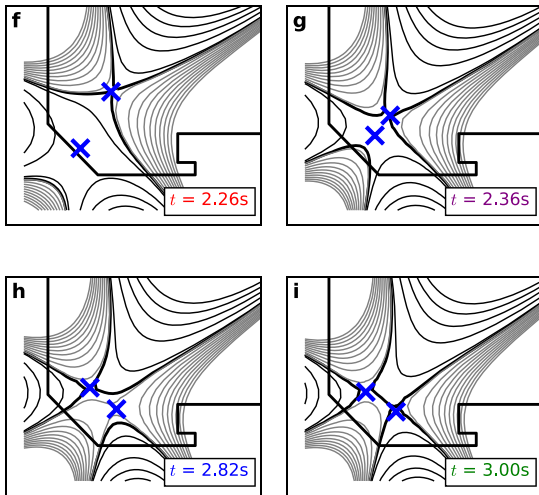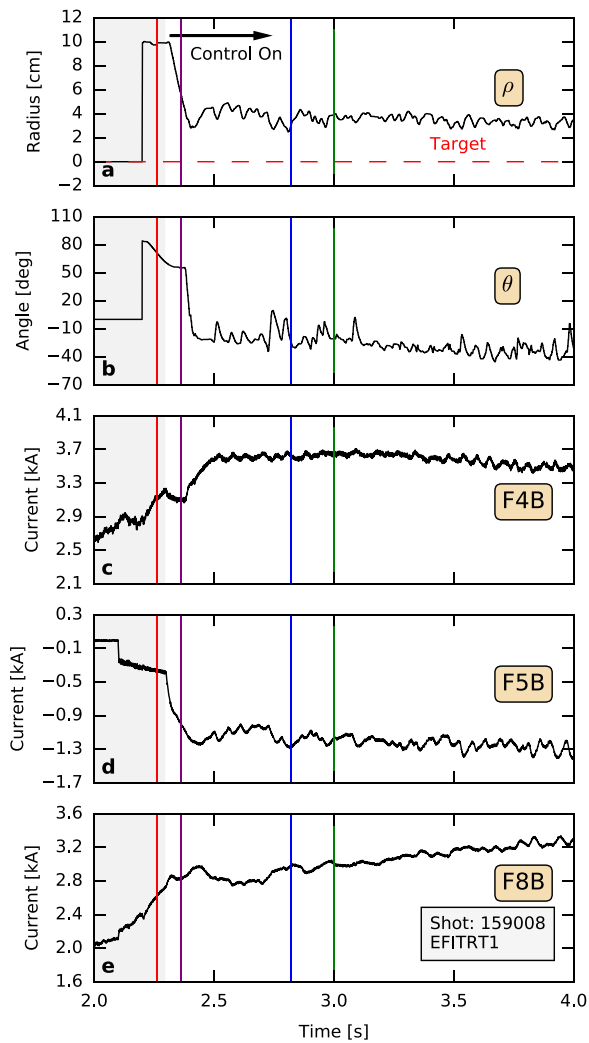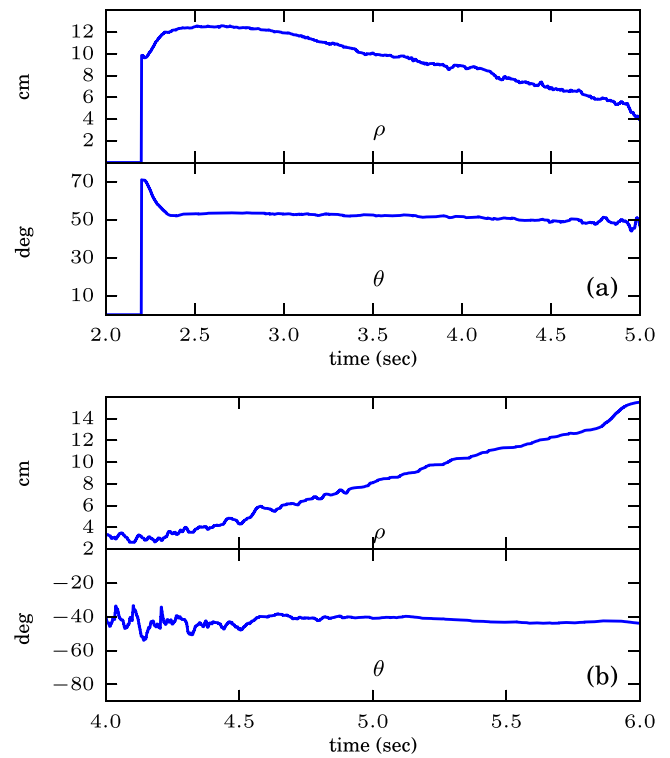
Figure 6. (*a*) (DIII–D shot 159021) Scan of the snowflake radius at a constant angle in the snowflake plus configuration. (*b*) (DIII–D shot 158955) Scan of the snowflake radius at a constant angle in the snowflake minus configuration.

The results in figure 5 also demonstrate the inherent ambiguity in our present algorithm for computing the snowflake angle. As shown in the figure, the snowflake angle as calculated in real-time was roughly constant at a value of $-40°$. According to the angle definition given in section 2.2, this suggests that the divertor configuration was a snowflake-minus throughout the discharge. However, we observed that the SFD configuration would transition between a low-field side SFD minus in which the secondary null was in the outboard scrape-off layer and a high-field side SFD minus in which the secondary null was in the inboard scrape-off layer, as illustrated in figures 5(*h*) and (*i*). While no attempt was made to control the snowflake angle in this particular discharge, the transitioning between the two snowflake-minus configurations is generally not desirable. In section 4, we discuss potential upgrades to the control algorithm that can address this problem.

Further tests were performed to demonstrate the multiple-input-multiple-output (MIMO) capabilities of the controller. In figure 6, we present the results of two shots in which the snowflake radius, ρ, and angle, θ, were simultaneously controlled. In these scenarios, the weighting matrix in (16) was programmed with two nonzero diagonal entries corresponding to the radius and angle. When performing combined radius-angle control, the angle was multiplied by the present value of the snowflake radius to generate a value for arc length having the same units as the radius. The use of equivalent units ensures that the controller distributes the control effort appropriately between the two quantities. Figure 6(*a*) shows the results of DIII–D shot 159021 in which the radius was
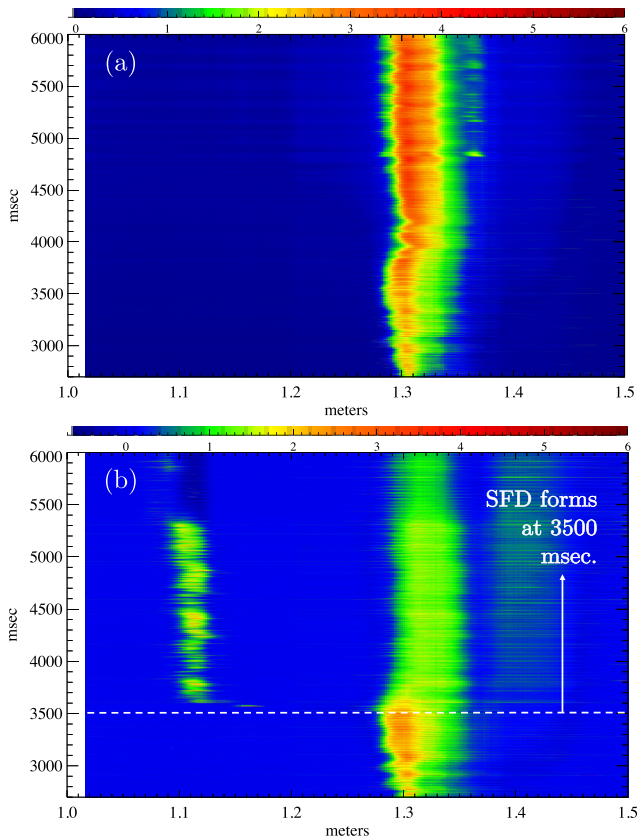

Figure 5. Results from DIII–D shot 159008 in which the control was used to achieve a near-exact SFD using PF coils F4B, F5B, and F8B. The control is enabled at $t = 2.3$ s. Plotted in frames (*a*) through (*e*) are the radius, angle, and the coil currents. Also shown are the divertor configurations at $t = 2.26$ s, 2.36 s, 2.82 s, and 3.00 s.

proportional-only control as well as to limitations originating from the finite resolution (2.3 cm $\times$ 4.6 cm) of the solution grid used by rtEFIT.

Figure 7. Heat flux profiles (W m^{-2}) on the lower divertor surface in DIII–D as measured by the infrared camera (IRTV) for (*a*) the advanced tokamak (AT) scenario with a LSN-biased double-null and (*b*) the AT scenario with a lower snowflake-minus. The horizontal axis represents the major radius (m) along the divertor surface, while the vertical axis represents time (ms). In DIII–D shot 155355, the SFD was formed at time ~3500 ms.

scanned at constant angle in the SFD-plus configuration, while figure 6(*b*) shows the results of DIII–D shot 158955 in which the radius was scanned in the SFD-minus configuration. We observed that the algorithm could maintain effective control of the radius and angle in both configurations. Minimal time was allocated for developing control of additional parameters such as the centroid coordinates. Utilization of the full MIMO capabilities of the controller will be an emphasis of forthcoming experiments.

Finally, the snowflake configuration was integrated into a double-null advanced tokamak (AT) scenario with $\beta_N \approx 3.0$ and $H_{98(y,2)} \approx 1.35$. In figure 7, we show the heat flux profiles on the surface of the lower divertor as measured by the infrared camera (IRTV) diagnostic in the AT scenario with a double single null standard divertor and a lower snowflake-minus. In shot 155355, the SFD was formed at time ~3.5 s. It is seen in the figure that there is a significant reduction in the heat flux (~2.5×) at the outer strike point location of ~135 cm subsequent to the formation of the SFD. Furthemore, an additional strike point, characteristic of the snowflake configuration, is clearly seen in the heat flux profile. The heat flux reduction was accompanied by a ~2.5× increase in the flux expansion when in the SFD configuration. The SFD configurations were maintained for many energy confinement times (2–3 s)

without any adverse effects on core plasma characteristics such as confinement. In addition, the radiative SFD regime was explored with gas seeding. Starting from attached conditions, plasma density was incrementally increased in consecutive plasma discharges in order to achieve detachment and radiative divertor conditions. The SFD control was shown to be robust under partial and full detachment conditions during these scans. A more detailed analysis of the physics results of these experiments can be found in [25, 26].

4. Conclusion

In this paper, we have presented an algorithm for realtime control of SFD configurations on DIII–D. The algorithm uses inputs from the realtime equilibrium reconstruction algorithm (rtEFIT) to locate the two magnetic nulls and then compute the coil currents required to achieve a desired SFD configuration. We provided experimental results to demonstrate the ability of the algorithm to control the distance between the nulls. It was then shown that implementing the SFD in an AT scenario allows a 2.5× reduction of the peak heat flux relative to the standard divertor.

Additional work is required to develop the control into a reliable and flexible system that can operate in a variety of scenarios. While control of the null point separation has been demonstrated, more work must be done to develop the multivariable control capabilities of the system. In order to achieve simultaneous control of the four snowflake shape descriptors, a more detailed analysis is needed of the appropriate weights and PID gains required and how these parameters depend upon the plasma scenario. In addition, we have identified a shortcoming of the current algorithm which is the inability of the algorithm to determine which of the two magnetic nulls of the snowflake divertor is the primary null on the separatrix. We are exploring several options to address this deficiency. One potential solution is to use the coordinates of the primary null as computed by the rtEFIT algorithm as an additional input to the snowflake control. This procedure has already been tested experimentally with success in tracking the primary null. We conclude by noting that our control scheme can be easily extended to include control of other divertor parameters such as the strike point location by augmenting the Jacobian matrix used for computation of the control coil currents. This provides a path forward for control development of other advanced divertors such as the X-divertor.

Appendix

In section 2.3, the Jacobian matrix, **J**, is used to compute the coil current requests that are required to achieve a desired SFD configuration in DIII–D. The Jacobian, which quantifies the effect on the snowflake position of modifying the coil currents, can be written explicitly in terms of its components as,

$$\mathbf{J} = \begin{bmatrix} \partial_{\mathbf{I}} r_c \\ \partial_{\mathbf{I}} z_c \\ \partial_{\mathbf{I}} \rho \\ \partial_{\mathbf{I}} \theta \end{bmatrix},$$

(A.1)

where the elements are computed row-by-row as follows,

$$\partial_{\mathbf{I}} r_c = \partial_{\mathbf{x}} \sigma_0 \cdot \partial_{\mathbf{B}} \mathbf{x} \cdot \partial_{\mathbf{I}} \mathbf{B},$$

(A.2a)

$$\partial_{\mathbf{I}} z_c = \partial_{\mathbf{x}} \zeta_0 \cdot \partial_{\mathbf{B}} \mathbf{x} \cdot \partial_{\mathbf{I}} \mathbf{B},$$

(A.2b)

$$\partial_{\mathbf{I}} \rho = \left(\partial_P \rho \cdot \partial_{\mathbf{x}} P + \partial_Q \rho \cdot \partial_{\mathbf{x}} Q \right) \cdot \partial_{\mathbf{B}} \mathbf{x} \cdot \partial_{\mathbf{I}} \mathbf{B},$$

(A.2c)

$$\partial_{\mathbf{I}} \theta = \left(\partial_P \theta \cdot \partial_{\mathbf{x}} P + \partial_Q \theta \cdot \partial_{\mathbf{x}} Q \right) \cdot \partial_{\mathbf{B}} \mathbf{x} \cdot \partial_{\mathbf{I}} \mathbf{B}.$$

(A.2d)

In this appendix, we provide analytical expressions for the various terms in (A.2a) through (A.2d). The magnetic field matrix $\partial_{\mathbf{I}} \mathbf{B}$ is computed using the Green's function of the Grad–Shafranov problem, as discussed in detail in section 2.3. No further comment on these derivatives is needed. The $\partial_{\mathbf{B}} \mathbf{x}$ matrix is easily computed as the inverse of the matrix that was used to compute the expansion coefficients from the field measurements in section 2.1.

Partial derivatives for r_c and z_c

$$\partial_{\mathbf{x}} \sigma_0 = \begin{bmatrix} \partial_{l_1} \sigma_0 & \partial_{l_2} \sigma_0 & \partial_{q_2} \sigma_0 & \partial_{q_3} \sigma_0 & \partial_{c_1} \sigma_0 & \partial_{c_4} \sigma_0 \end{bmatrix},$$

(A.3)

where the components of $\partial_{\mathbf{x}} \sigma_0$ are defined as,

$$\frac{\partial \sigma_0}{\partial l_1} = 0,$$

(A.4a)

$$\frac{\partial \sigma_0}{\partial l_2} = 0,$$

(A.4b)

$$\frac{\partial \sigma_0}{\partial q_2} = \frac{c_4}{3 \left(c_1^2 + c_4^2 \right)},$$

(A.4c)

$$\frac{\partial \sigma_0}{\partial q_3} = \frac{c_1}{3 \left(c_1^2 + c_4^2 \right)},$$

(A.4d)

$$\frac{\partial \sigma_0}{\partial c_1} = -\frac{2 q_2 c_1 c_4 + q_3 \left(c_1^2 - c_4^2 \right)}{3 \left(c_1^2 + c_4^2 \right)^2},$$

(A.4e)

$$\frac{\partial \sigma_0}{\partial c_4} = -\frac{2 q_3 c_1 c_4 - q_2 \left(c_1^2 - c_4^2 \right)}{3 \left(c_1^2 + c_4^2 \right)^2}.$$

(A.4f)

$$\partial_{\mathbf{x}} \zeta_0 = \begin{bmatrix} \partial_{l_1} \zeta_0 & \partial_{l_2} \zeta_0 & \partial_{q_2} \zeta_0 & \partial_{q_3} \zeta_0 & \partial_{c_1} \zeta_0 & \partial_{c_4} \zeta_0 \end{bmatrix},$$

(A.5)

where the components of $\partial_{\mathbf{x}} \zeta_0$ are defined as follows,

$$\frac{\partial \zeta_0}{\partial l_1} = 0,$$

(A.6a)

$$\frac{\partial \zeta_0}{\partial l_2} = 0,$$

(A.6b)

$$\frac{\partial \zeta_0}{\partial q_2} = \frac{c_1}{3 \left(c_1^2 + c_4^2 \right)},$$

(A.6c)

$$\frac{\partial \zeta_0}{\partial q_3} = -\frac{c_4}{3 \left(c_1^2 + c_4^2 \right)},$$

(A.6d)

$$\frac{\partial \zeta_0}{\partial c_1} = \frac{2 q_3 c_1 c_4 - q_2 \left(c_1^2 - c_4^2 \right)}{3 \left(c_1^2 + c_4^2 \right)^2},$$

(A.6e)

$$\frac{\partial \zeta_0}{\partial c_4} = -\frac{2 q_2 c_1 c_4 + q_3 \left(c_1^2 - c_4^2 \right)}{3 \left(c_1^2 + c_4^2 \right)^2}.$$

(A.6f)

Partial derivatives for ρ and θ

$$\partial_{\mathbf{x}} P = \begin{bmatrix} \partial_{l_1} P & \partial_{l_2} P & \partial_{q_2} P & \partial_{q_3} P & \partial_{c_1} P & \partial_{c_4} P \end{bmatrix},$$

(A.7)

where the components of $\partial_{\mathbf{x}} P$ are defined as follows,

$$\frac{\partial P}{\partial l_1} = -\frac{c_1}{3 \left(c_1^2 + c_4^2 \right)},$$

(A.8a)

$$\frac{\partial P}{\partial l_2} = \frac{c_4}{3 \left(c_1^2 + c_4^2 \right)},$$

(A.8b)

$$\frac{\partial P}{\partial q_2} = \frac{2 \left(q_2 \left(c_4^2 - c_1^2 \right) + 2 q_3 c_1 c_4 \right)}{9 \left(c_1^2 + c_4^2 \right)^2},$$

(A.8c)

$$\frac{\partial P}{\partial q_3} = \frac{2 \left(q_3 \left(c_1^2 - c_4^2 \right) + 2 q_2 c_1 c_4 \right)}{9 \left(c_1^2 + c_4^2 \right)^2},$$

(A.8d)

$$\frac{\partial P}{\partial c_1} = \frac{1}{9 \left(c_1^2 + c_4^2 \right)^3} \Big[3 l_1 \left(c_1^4 - c_4^4 \right) - 4 q_2 q_3 c_4 \left(3 c_1^2 - c_4^2 \right) + 2 c_1 \left(q_2^2 - q_3^2 \right) \left(c_1^2 - 3 c_4^2 \right) - 6 l_2 c_1 c_4 \left(c_1^2 + c_4^2 \right) \Big],$$

(A.8e)

$$\frac{\partial P}{\partial c_4} = \frac{1}{9 \left(c_1^2 + c_4^2 \right)^3} \Big[3 l_2 \left(c_1^4 - c_4^4 \right) - 4 q_2 q_3 c_1 \left(c_1^2 - 3 c_4^2 \right) + 2 c_4 \left(q_2^2 - q_3^2 \right) \left(3 c_1^2 - c_4^2 \right) + 6 l_1 c_1 c_4 \left(c_1^2 + c_4^2 \right) \Big].$$

(A.8f)

$$\partial_{\mathbf{x}} Q = \begin{bmatrix} \partial_{l_1} Q & \partial_{l_2} Q & \partial_{q_2} Q & \partial_{q_3} Q & \partial_{c_1} Q & \partial_{c_4} Q \end{bmatrix},$$

(A.9)

where the components of $\partial_{\mathbf{x}} Q$ are defined as follows,

$$\frac{\partial Q}{\partial l_1} = \frac{c_4}{6 \left(c_1^2 + c_4^2 \right)},$$

(A.10a)

$$\frac{\partial Q}{\partial l_2} = \frac{c_1}{6 \left(c_1^2 + c_4^2 \right)},$$

(A.10b)

$$\frac{\partial Q}{\partial q_2} = \frac{q_3 \left(c_1^2 - c_4^2 \right) + 2 q_2 c_1 c_4}{9 \left(c_1^2 + c_4^2 \right)^2},$$

(A.10c)

$$\frac{\partial Q}{\partial q_3} = \frac{q_2\left(c_1^2 - c_4^2\right) - 2q_3 c_1 c_4}{9\left(c_1^2 + c_4^2\right)^2}, \tag{A.10d}$$

$$\frac{\partial Q}{\partial c_1} = \frac{1}{18\left(c_1^2 + c_4^2\right)^3}\Big[-3l_2\left(c_1^4 - c_4^4\right) - 4q_2 q_3 c_1\left(c_1^2 - 3c_4^2\right)$$
$$- 2c_4\left(q_2^2 - q_3^2\right)\left(3c_1^2 - c_4^2\right) - 6l_1 c_1 c_4\left(c_1^2 + c_4^2\right)\Big], \tag{A.10e}$$

$$\frac{\partial Q}{\partial c_4} = \frac{1}{18\left(c_1^2 + c_4^2\right)^3}\Big[3l_1\left(c_1^4 - c_4^4\right) - 4q_2 q_3 c_4\left(3c_1^2 - c_4^2\right)$$
$$+ 2c_1\left(q_2^2 - q_3^2\right)\left(c_1^2 - 3c_4^2\right) - 6l_2 c_1 c_4\left(c_1^2 + c_4^2\right)\Big]. \tag{A.10f}$$

Furthermore, $\partial_P \rho$ and $\partial_Q \rho$ are written as,

$$\frac{\partial \rho}{\partial P} = \frac{P}{2\left(P^2 + 4Q^2\right)^{3/4}}, \tag{A.11a}$$

$$\frac{\partial \rho}{\partial Q} = \frac{2Q}{\left(P^2 + 4Q^2\right)^{3/4}}. \tag{A.11b}$$

Finally, $\partial_P \theta$ and $\partial_Q \theta$ are computed in the same manner as equations (25) by differentiating equation (12d).

ORCID iDs

A.W. Leonard ⬡ https://orcid.org/0000-0001-9356-1074
E.A. Unterberg ⬡ https://orcid.org/0000-0003-1353-8865

References

[1] Wischmeier M. (The ASDEX Upgrade Team and JET EFDA Contributors) 2015 *J. Nucl. Mater.* **463** 22
[2] Ikeda K. 2007 *Nucl. Fusion* **47**
[3] Garofalo A.M. *et al* 2014 *Nucl. Fusion* **54** 073015
[4] Menard J. *et al* 2012 Progress on developing the spherical tokamak for fusion applications *Proc. 24th IAEA FEC (San Diego, CA)* (www-naweb.iaea.org/napc/physics/FEC/FEC2012/papers/379_FTP34.pdf)
[5] Zohm H. 2013 *Nucl. Fusion* **53** 073019
[6] Ryutov D.D. 2007 *Phys. Plasmas* **14** 064502
[7] Kotschenreuther M., Valanju P., Covele B. and Mahajan S. 2013 *Phys. Plasmas* **20** 102507
[8] Valanju P.M., Kotschenreuther M., Mahajan S.M. and Canik J. 2009 *Phys. Plasmas* **16** 056110
[9] LaBombard B. 2014 *Bull. Am. Phys. Soc.* **58** 16
[10] Piras F. 2009 *Plasma Phys. Control. Fusion* **51** 055009
[11] Soukhanovskii V.A. *et al* 2012 *Phys. Plasmas* **19** 082504
[12] Calabrò G. *et al* 2015 *Nucl. Fusion* **55** 083005
[13] Asakura N. *et al* 2013 *Fusion Sci. Technol.* **63** 70
[14] Luo Z.P., Xiao B.J., Guo Y. and Ye M.Y. 2013 Optimization of the snowflake diverted equilibria in cfetr *Proc. 2013 IEEE 25th Symp. on Fusion Engineering (San Francisco, CA)* (https://doi.org/10.1109/SOFE.2013.6635420)
[15] Ryutov D.D. and Soukhanovskii V.A. 2015 *Phys. Plasmas* **22** 110901
[16] Walker M.L., Humphreys D.A. and Ferron J.R. 1997 Control of plasma poloidal shape and position in the DIII-D tokamak *Proc. 36th Conf. on Decision & Control (San Diego, CA)* (https://doi.org/10.1109/CDC.1997.652432)
[17] Ferron J.R., Walker M.L., Lao L.L., St. John H.E., Humphreys D.A. and Leuer J.A. 1998 *Nucl. Fusion* **38** 1055
[18] Kolemen E., Gates D.A., Rowley C.W., Kasdin N.J., Kallman J., Gerhardt S., Soukhanovskii V. and Mueller D. 2010 *Nucl. Fusion* **50** 105010
[19] Kolemen E., Gates D.A., Gerhardt S., Kaita R., Kugel H., Mueller D., Rowley C. and Soukhanovskii V. 2011 *Nucl. Fusion* **51** 113024
[20] Boyer M.D. *et al* 2018 *Nucl. Fusion* **58** 036016
[21] Ryutov D.D., Makowski M.A. and Umansky M.V. 2010 *Plasma Phys. Control. Fusion* **52** 105001
[22] Ogata K. 2010 *Modern Control Engineering* 5th edn (Englewood Cliffs, NJ: Prentice Hall)
[23] Bechhoefer J. 2005 *Rev. Mod. Phys.* **77** 783
[24] Ryutov D.D., Cohen R.H., Farmer W.A., Rognlien T.D. and Umansky M.V. 2014 *Phys. Scr.* **89** 088002
[25] Petrie T.W. *et al* 2015 *J. Nucl. Mater.* **463** 1225
[26] Soukhanovskii V.A. *et al* 2015 *J. Nucl. Mater.* **463** 1191